



OPEN

# High-temperature optical properties of indium tin oxide thin-films

Jiwoong Kim<sup>1,2</sup>, Sujan Shrestha<sup>1</sup>, Maryam Souri<sup>1</sup>, John G. Connell<sup>1</sup>, Sungkyun Park<sup>2</sup> & Ambrose Seo<sup>1</sup>✉

Indium tin oxide (ITO) is one of the most widely used transparent conductors in optoelectronic device applications. We investigated the optical properties of ITO thin films at high temperatures up to 800 °C using spectroscopic ellipsometry. As temperature increases, amorphous ITO thin films undergo a phase transition at ~200 °C and develop polycrystalline phases with increased optical gap energies. The optical gap energies of both polycrystalline and epitaxial ITO thin films decrease with increasing temperature due to electron–phonon interactions. Depending on the background oxygen partial pressure, however, we observed that the optical gap energies exhibit reversible changes, implying that the oxidation and reduction processes occur vigorously due to the low oxidation and reduction potential energies of the ITO thin films at high temperatures. This result suggests that the electronic structure of ITO thin films strongly depends on temperature and oxygen partial pressure while they remain optically transparent, i.e., optical gap energies > 3.6 eV.

Tin-doped indium oxide or indium tin oxide (ITO) is a transparent conductor, which is widely used in modern optoelectronic devices such as thin-film transistors, resistive switching memories, and solar cells<sup>1–5</sup>. However, it is mostly unexplored if its high electrical conductivity and optical transparency will remain intact at extreme conditions such as high temperature or pressure. The question concerning the high-temperature property of materials is particularly important as modern technology evolves to device applications and operations in harsh environments above 500 °C<sup>6–8</sup>. Since the bandgap energies of semiconductors usually decrease with increasing temperature<sup>9,10</sup>, we may expect that ITO will also lose its optical transparency at high temperatures. Indeed, indium oxide (In<sub>2</sub>O<sub>3</sub>) single crystals have been reported to show a more significant reduction of its optical gap at high temperatures than semiconductor crystals such as Si and GaAs<sup>11</sup>. This somewhat pessimistic result is understood by a strong interaction between electrons and lattice vibrations (i.e., electron–phonon interaction), affecting the bandgap energy of In<sub>2</sub>O<sub>3</sub><sup>12</sup>. However, it is essential to note that high concentrations of doped Sn ions and oxygen vacancies play a crucial role in the electronic band structure of ITO and its optical properties. For example, the optical gap energy of ITO is larger than that of undoped In<sub>2</sub>O<sub>3</sub> because of the existence of free electron carriers<sup>13</sup>, according to the Burstein–Moss effect<sup>14</sup>, and the temperature dependence of free carrier concentration is nearly constant<sup>15</sup>. Hence, investigating the high-temperature optical properties of ITO requires systematic measurements and understanding of the role of dopants and defects as well as electron–phonon interactions.

In this paper, we report the high-temperature optical properties of ITO thin films up to 800 °C. We studied ITO thin films of amorphous (*a*-ITO), polycrystalline (*poly*-ITO), and epitaxial (*epi*-ITO) phases rather than ITO bulk crystals because these thin-film forms are the ones used in various optoelectronic device applications. While *a*-ITO thin films show an abrupt increase of optical gap energies due to crystallization at ~200 °C, the optical gap energies of *poly*-ITO and *epi*-ITO thin films decrease gradually as temperature increases. Nevertheless, the optical gap energies ( $E_g$ ) remain higher than the visible photon energies (i.e.,  $E_g > 3$  eV), meaning that their optical transparency is unaffected. We also found that background oxygen partial pressure at high temperatures alters the optical gap energies of ITO thin films *reversibly* by oxidation and reduction processes. Our results demonstrate that an unintentional oxygen annealing effect at high temperatures can result in different optical and transport properties of ITO thin films.

<sup>1</sup>Department of Physics and Astronomy, University of Kentucky, Lexington, KY 40506, USA. <sup>2</sup>Department of Physics, Pusan National University, Busan 46241, Korea. ✉email: a.seo@uky.edu

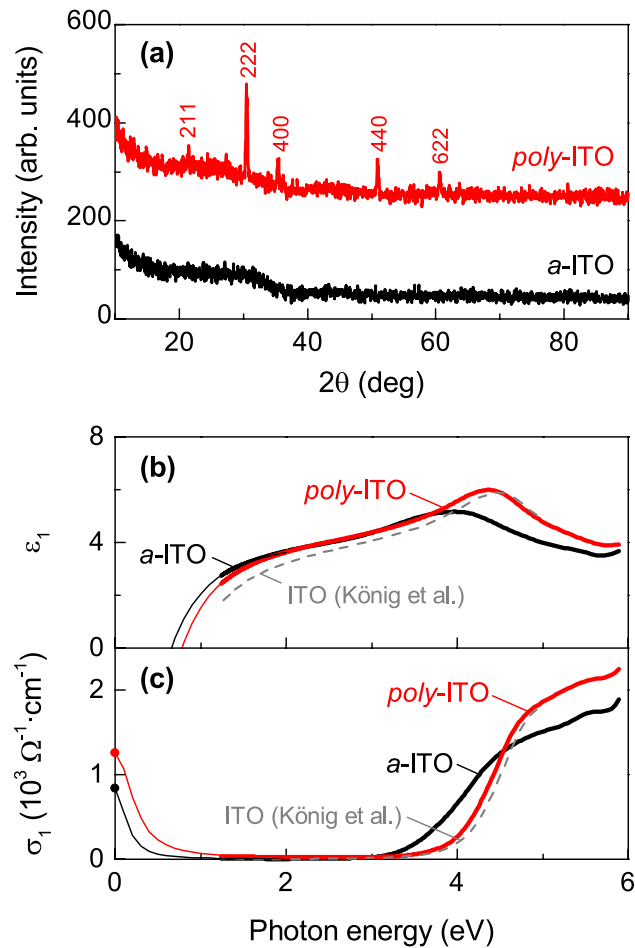


**Figure 1.** Structural and optical characterization of *a*-ITO and *poly*-ITO thin films. **(a)** XRD  $\theta$ - $2\theta$  scans of *a*-ITO (black) and *poly*-ITO (red) thin films. According to the diffraction indices of *poly*-ITO, it is a cubic bixbyite structure (ICSD #50848). **(b)** Dielectric constant ( $\epsilon_1$ ) and **(c)** optical conductivity ( $\sigma_1$ ) spectra of *a*-ITO (black) and *poly*-ITO (red) thin films measured at room temperature. The grey dashed lines are the spectra from Ref.<sup>33</sup> for comparison. The dots at zero photon energy are from *dc*-conductivity measurements. The solid thin lines between 0 and 1.2 eV are interpolated using the Drude model.

## Results and discussion

### Amorphous and polycrystalline ITO thin films.

We observed that *a*-ITO thin films undergo a phase transition in the annealing process and develop a polycrystalline phase with increased  $E_g$  at high temperatures. Figure 1a shows X-ray diffraction (XRD)  $\theta$ - $2\theta$  scans of both as-grown *a*-ITO and *poly*-ITO, which are ITO thin films on glass substrates before and after post-annealing at 500 °C, respectively. While the *a*-ITO thin film shows no visible peak, which verifies that the thin film is amorphous, clear diffraction peaks appear in the annealed sample. The diffraction peaks of the *poly*-ITO thin film match well with the cubic bixbyite ITO structure (ICSD #50848). Note that *poly*-ITO thin films exhibit a larger  $E_g$  (i.e.,  $4.25 \pm 0.01$  eV) than *a*-ITO thin films (i.e.,  $3.85 \pm 0.01$  eV) at room temperature, as shown in Fig. 1b,c. The relation between the complex dielectric function ( $\tilde{\epsilon} = \tilde{n}^2 = \epsilon_1 + i\epsilon_2$ ), and the optical conductivity ( $\sigma_1$ ) is  $\sigma_1 = \frac{\epsilon_2\omega}{4\pi}$ , where  $\omega$  is the photon energy. The spectral shapes of  $\epsilon_1$  and  $\sigma_1$  and the change of  $E_g$  are consistent with each other according to the Kramers-Kronig relation. We extrapolated the spectra below 1.2 eV using the Drude model<sup>16</sup> to match with the *dc* conductivities (i.e.,  $\sigma_1$  at 0 eV) of these samples. The estimated plasma frequencies, where the dielectric constant crosses zero, increase from  $0.7 \pm 0.1$  eV (*a*-ITO) to  $0.8 \pm 0.1$  eV (*poly*-ITO). Since the plasma frequency ( $\omega_p$ ) is proportional to the carrier concentration ( $n_c$ ) ( $\omega_p^2 = 4\pi n_c e^2/m$ , where  $e$  and  $m$  are the elementary charge and the effective mass of electron, respectively), the enhanced  $E_g$  in *poly*-ITO thin films is presumably due to increased free carriers (i.e., the Burstein-Moss effect<sup>14</sup>) and reduced disorder<sup>17</sup>.

To determine high-temperature  $E_g$  of *a*-ITO and *poly*-ITO thin films, we calculated the absorption coefficient ( $\alpha$ ) from the extinction coefficient ( $k$ ) using  $\alpha = 4\pi k/\lambda$ , where  $\lambda$  is the wavelength of the photon. Since the direct  $E_g$  has the relation:  $\alpha \approx (\omega - E_g)^{1/2}$  (Ref.<sup>14</sup>), Figure 2a,b shows  $\alpha^2$  vs. photon energy plots of *a*-ITO and *poly*-ITO thin films above room temperature, respectively.  $E_g$  is estimated by linear extrapolation at each temperature. Figure 2c shows  $E_g$  as a function of temperature for both *a*-ITO and *poly*-ITO thin films. Note that  $E_g$  of *a*-ITO thin films shows an abrupt change above 200 °C, where polycrystalline ITO starts forming, as reported in

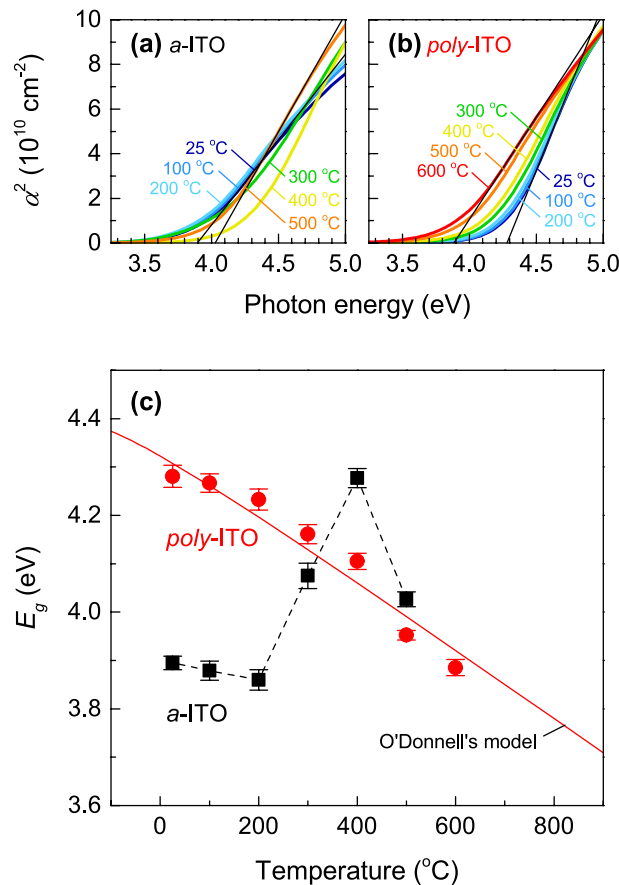


**Figure 2.** High-temperature optical properties of *a*-ITO and *poly*-ITO thin films. Absorption coefficient squared ( $\alpha^2$ ) vs. photon energy plots for (a) *a*-ITO and (b) *poly*-ITO thin films obtained from ellipsometry spectra at high temperatures up to 500 °C and 600 °C, respectively. The black lines are the linear extrapolation of  $\alpha^2$  spectra at 25 °C and 500 °C (600 °C) for the *a*-ITO (*poly*-ITO) thin film. (c) Optical gap energies of *a*-ITO and *poly*-ITO thin films as a function of temperature. The solid red line is a curve fit from O'Donnell's model<sup>10</sup>.

Refs.<sup>18,19</sup>. On the other hand,  $E_g$  of *poly*-ITO thin films decreases gradually with increasing temperature, as also shown in Fig. 2c. We suggest that strong electron–phonon interaction of *poly*-ITO thin films is responsible for the temperature dependence of  $E_g$ . According to O'Donnell's model<sup>10</sup>,  $E_g$  at absolute temperature  $T$  is described by

$$E_g(T) = E_g(0) - S \langle \hbar\omega_{ph} \rangle \left[ \coth \left( \frac{\langle \hbar\omega_{ph} \rangle}{2k_B T} \right) - 1 \right], \quad (1)$$

where  $S$  is a dimensionless coupling constant,  $\langle \hbar\omega_{ph} \rangle$  is the average phonon energy, and  $k_B$  is the Boltzmann constant. Using the average phonon energy of  $\text{In}_2\text{O}_3$  (38.6 meV)<sup>11</sup>, we can obtain  $E_g(0) = 4.40 \pm 0.04$  eV and  $S = 4.2 \pm 0.5$ , as shown in Fig. 2c (red line). Note that the coupling constant  $S$  is smaller than that of undoped  $\text{In}_2\text{O}_3$  ( $S = 8.24$ )<sup>11</sup>, implying that lattice imperfections such as substitutional Sn ions, oxygen vacancies, and grain boundaries, at which phonons are scattered<sup>20</sup>, suppress the electron–phonon interactions in *poly*-ITO thin films.

**Epitaxial ITO thin films.** To explore intrinsic high-temperature optical properties, we measured *epi*-ITO thin films prepared in two different annealing conditions, i.e.,  $p(\text{O}_2) = 10$  mTorr ( $\text{O}_2$ -annealed) and  $p(\text{O}_2) < 1.0 \times 10^{-6}$  Torr (vacuum-annealed). Figure 3a,b shows XRD  $\theta$ - $2\theta$  scans and reciprocal space mappings, respectively. Both *epi*-ITO thin films are coherently grown without any notable secondary phases. It is noteworthy that these samples show identical in-plane ( $10.25 \pm 0.01$  Å) and out-of-plane lattice constants ( $10.07 \pm 0.01$  Å) regardless of the annealing conditions. The *epi*-ITO thin films are under tensile strain ( $\sim 1.3\%$ ) due to the lattice mismatch with YSZ substrates<sup>21</sup>. However, the room-temperature optical spectra of *epi*-ITO thin films strongly depend on the annealing conditions presumably due to different concentrations of oxygen vacancies. It was found that the carrier concentration of  $\text{In}_2\text{O}_3$  thin films decreased as increasing the  $\text{O}_2$  pressure during growth<sup>22,23</sup>. DFT calculations suggested that the oxygen vacancies are shallow donors in  $\text{In}_2\text{O}_3$ , contributing to the carrier concentration<sup>24,25</sup>. Figure 3c shows  $\epsilon_1$  and  $\sigma_1$  spectra of *epi*-ITO thin films, respectively. The vacuum-annealed *epi*-ITO thin film shows both increased  $\omega_p$  ( $0.8 \pm 0.1$  eV) and  $E_g$  (i.e.,  $4.26 \pm 0.03$  eV) compared to the  $\text{O}_2$ -annealed *epi*-ITO thin film ( $\omega_p = 0.5 \pm 0.1$  eV and  $E_g = 4.00 \pm 0.05$  eV). This observation is consistent with the Burstein–Moss effect<sup>14</sup> since larger free carrier concentrations result in higher  $E_g$  values. Therefore, the annealing

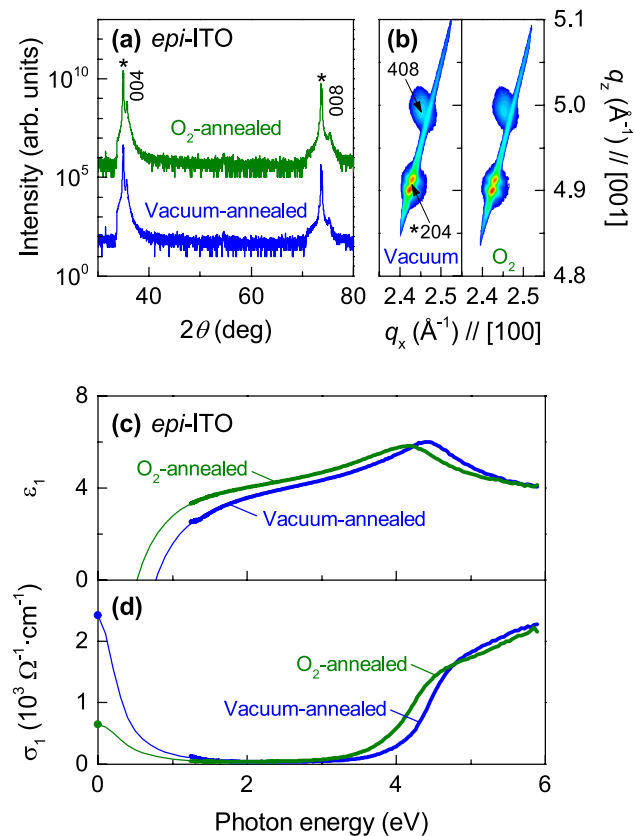


**Figure 3.** Structural and optical characterization of *epi*-ITO thin films. (a) XRD  $\theta$ - $2\theta$  scans of *epi*-ITO thin films annealed in O<sub>2</sub> (green) and vacuum (blue) conditions. The asterisks (\*) and the indices denote the peaks from the YSZ substrate and cubic bixbyite ITO thin films, respectively. (b) X-ray reciprocal space maps near the 204-reflection of YSZ. Both samples show clear 408-reflections from *epi*-ITO thin films. (c)  $\epsilon_1$  and (d)  $\sigma_1$  spectra of vacuum-annealed and O<sub>2</sub>-annealed *epi*-ITO thin films at room temperature. The dots at zero photon energy are from *dc*-conductivity measurements. The solid thin lines between 0 and 1.2 eV are interpolated using the Drude model.

conditions influence the number of oxygen vacancies, which are electrons donors<sup>13</sup>, and increase (decrease) the carrier concentrations by reducing (oxidizing) *epi*-ITO thin films and change their optical properties without any noticeable difference in the crystal structure.

We measured  $E_g$  of *epi*-ITO thin films at high temperatures while maintaining the same environmental conditions as the post-annealing process. Figure 4a,b shows  $\alpha^2$  vs. photon energy plots for vacuum-annealed and O<sub>2</sub>-annealed *epi*-ITO thin films, respectively. Figure 4c shows  $E_g$  of *epi*-ITO thin films as a function of temperature obtained from the spectra. Note that both samples show systematically decreasing  $E_g$  with increasing temperature. Based on the average phonon energy of In<sub>2</sub>O<sub>3</sub> (38.6 meV)<sup>11</sup>, we find  $E_g(0) = 4.33 \pm 0.01$  eV and  $S = 3.0 \pm 0.1$  for the vacuum-annealed *epi*-ITO thin film and  $E_g(0) = 4.10 \pm 0.02$  eV and  $S = 3.6 \pm 0.3$  for the O<sub>2</sub>-annealed *epi*-ITO thin film. Interestingly, the O<sub>2</sub>-annealed *epi*-ITO shows an almost constant  $E_g$  above 600 °C. We speculate that these steady  $E_g$  values above 600 °C are related to the phase transition of In<sub>2</sub>O<sub>3</sub> from a cubic bixbyite structure to a rhombohedral corundum structure<sup>26</sup> because the  $E_g$  of corundum phase (3.8 eV)<sup>27</sup> is higher than bixbyite phase (2.7 eV)<sup>11</sup> at room temperature. However, it should be checked by high-temperature structural characterizations in future studies.

**Oxidation and reduction of ITO thin films at high temperatures.** We observed that reversible oxidation and reduction processes affect  $E_g$  of *epi*-ITO thin films at high temperatures. Figure 5 shows temperature-dependent  $E_g$  of vacuum-annealed or O<sub>2</sub>-annealed *epi*-ITO thin films measured under the conditions of vacuum ( $p(\text{O}_2) < 1.0 \times 10^{-6}$  Torr) or oxygen ( $p(\text{O}_2) = 10$  mTorr). When the vacuum-annealed *epi*-ITO thin film is placed under the vacuum environment (Fig. 5a), its  $E_g$  shows identical temperature-dependence during the heating and cooling cycles. However, when the sample is under the oxygen environment (Fig. 5b), its  $E_g$  decreases significantly at around 300 °C during the heating process, and its  $E_g$  becomes about 0.23 eV smaller than the initial  $E_g$  after cooling down to room temperature. This observation indicates that exposure to high temperatures above 300 °C oxidizes *epi*-ITO thin films and reduces free electron carriers.

In contrast, when the O<sub>2</sub>-annealed *epi*-ITO thin film is located under the vacuum condition, its  $E_g$  at room temperature increases about 0.24 eV after the heating and cooling cycle (Fig. 5c) whereas its  $E_g$  does not change

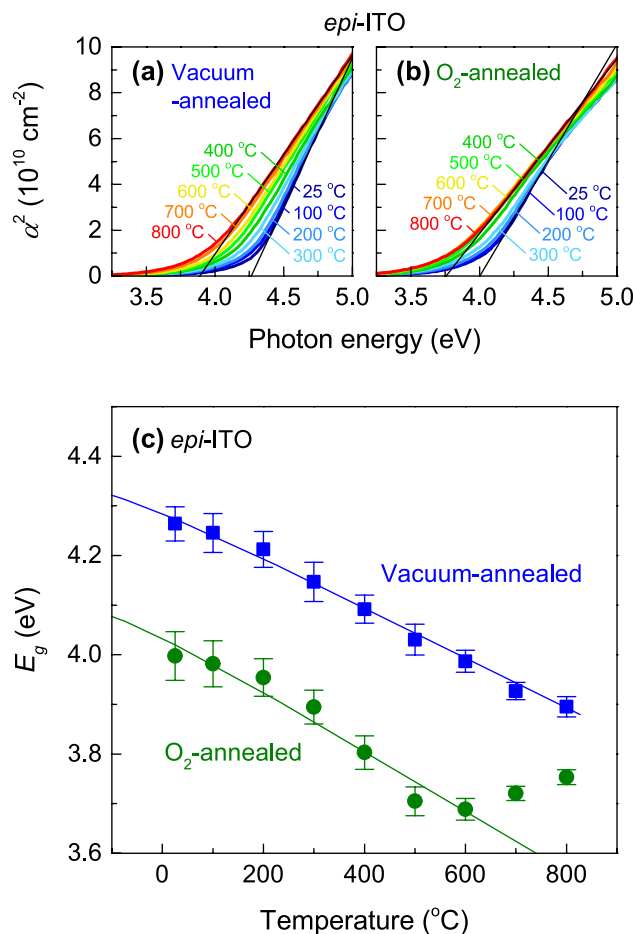


**Figure 4.** High-temperature optical properties of *epi*-ITO thin films.  $\alpha^2$  vs. photon energy plots for (a) vacuum-annealed and (b)  $O_2$ -annealed *epi*-ITO thin films obtained from ellipsometry spectra at high temperatures up to 800 °C. The black lines show the linear extrapolation of  $\alpha^2$  spectra at 25 °C and 800 °C. (c) Optical gap energies of vacuum-annealed and  $O_2$ -annealed *epi*-ITO thin films as a function of temperature. The blue and green lines are curve fits of vacuum-annealed and  $O_2$ -annealed *epi*-ITO thin films, respectively, using O'Donnell's model<sup>10</sup>.

after the thermal cycling under the  $O_2$  environment (Fig. 5d). The increased  $E_g$  under the vacuum condition reveals that oxygen vacancies and free-electron carriers are generated at high temperatures. Therefore, we can see that the background oxygen partial pressure at high temperatures affect the number of oxygen vacancies, which alters  $E_g$  of *epi*-ITO thin films. Note that the change of  $E_g$  is reversible (compare Fig. 5b with Fig. 5c), meaning that the oxidation and reduction potential energies of the ITO thin films are so low that oxidation and reduction processes occur vigorously at high temperatures.

## Conclusion

We have investigated the optical properties of ITO thin films at high temperatures using SE. The *a*-ITO thin films undergo a phase transition from amorphous to polycrystalline above 200 °C, and its  $E_g$  increases during the transition due to increased free carriers and reduced disorder. The *poly*-ITO and *epi*-ITO thin films exhibit a decrease in  $E_g$  with increasing temperature due to electron-phonon interactions. By monitoring  $E_g$  of *epi*-ITO thin films, we have observed that the oxidation and reduction processes occur reversibly at high temperatures depending on background oxygen partial pressure. All ITO thin films exhibit  $E_g$  higher than 3.5 eV up to 800 °C despite various changes in their electronic structures, suggesting that ITO thin films possess robust optical transparency for high-temperature device applications.

## Methods

We synthesized *a*-ITO and *poly*-ITO thin films grown on glass substrates. The *a*-ITO thin films were grown by using the *dc*-magnetron sputtering technique with a mixture gas of Ar and  $O_2$ . The as-grown *a*-ITO thin films were crystallized into *poly*-ITO thin films after annealing at 500 °C under  $O_2$  environment ( $p(O_2) = 10$  mTorr). We fabricated the *epi*-ITO thin films on yttria-stabilized zirconia (YSZ)  $Y:ZrO_2$  (001) substrates using pulsed laser deposition (PLD). The PLD conditions were the oxygen partial pressure ( $p(O_2)$ ) of 10 mTorr, and the laser (KrF excimer laser ( $\lambda = 248$  nm)) influence of 1.5 J/cm<sup>2</sup> with the repetition rate of 10 Hz. The substrate temperature

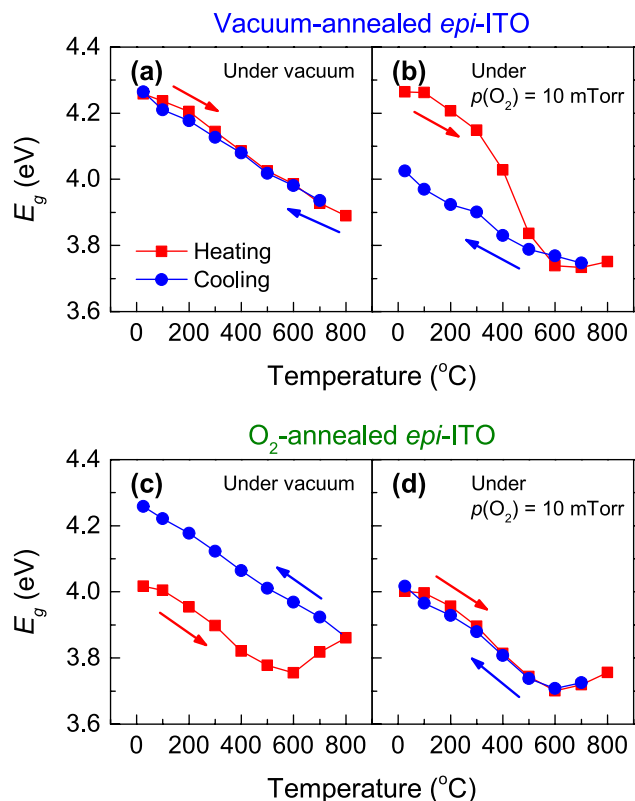


**Figure 5.** Optical gap energies of *epi*-ITO thin films during oxidation and reduction processes. The vacuum-annealed *epi*-ITO thin film is exposed to (a) vacuum and (b)  $p(\text{O}_2) = 10$  mTorr during the thermal cycle. The  $\text{O}_2$ -annealed *epi*-ITO thin film is exposed to (c) vacuum and (d)  $p(\text{O}_2) = 10$  mTorr during the thermal cycle. The red and blue arrows indicate the directions of heating and cooling processes, respectively.

was 600 °C to grow high crystalline *epi*-ITO thin film<sup>28</sup>. After the *epi*-ITO thin film growth, the samples were annealed under vacuum ( $p(\text{O}_2) < 1.0 \times 10^{-6}$  Torr) and  $\text{O}_2$  ( $p(\text{O}_2) = 10$  mTorr) environments, respectively, to control oxygen vacancies inside the thin films. Table S1 summarizes the growth condition of various ITO thin films in this study. We performed optical spectroscopic measurements with photon energies from 1.2 to 6.0 eV using a spectroscopic ellipsometer (Woollam M-2000) equipped with a custom-built vacuum chamber<sup>29</sup> with an incident angle of 65° at high temperatures. We measured *a*-ITO (*poly*-ITO) thin films at  $p(\text{O}_2) = 10$  mTorr up to 500 °C (600 °C) before the glass substrate is deformed<sup>30</sup>. For *epi*-ITO thin films, we measured up to 800 °C under vacuum ( $p(\text{O}_2) < 1.0 \times 10^{-6}$  Torr) and oxygen ( $p(\text{O}_2) = 10$  mTorr) environments. We extracted the complex refractive index,  $\tilde{n} = n + ik$ , where  $n$  and  $k$  are the refractive index and the extinction coefficient, respectively, from the measured spectroscopic ellipsometry parameters,  $\Psi$  and  $\Delta$ , which are the amplitude ratio and phase difference<sup>31</sup>, using numerical interaction process based on the Fresnel equation<sup>32</sup>. (See the Supplementary material for details.) We used a single slab model, i.e., air/ITO/YSZ, without any correction of surface roughness.

Received: 7 March 2020; Accepted: 19 June 2020

Published online: 27 July 2020

## References

- Qian, K., Han, X., Li, H., Chen, T. & Lee, P. S. Uncovering the indium filament revolution in transparent bipolar ITO/SiO<sub>x</sub>/ITO resistive switching memories. *ACS Appl. Mater. Interfaces* **12**, 4579–4585 (2020).
- Lin, Y. *et al.* 17% Efficient organic solar cells based on liquid exfoliated WS<sub>2</sub> as a replacement for PEDOT:PSS. *Adv. Mater.* **31**, 1902965 (2019).
- Liu, Z. *et al.* Flexible indium-tin-oxide homojunction thin-film transistors with two in-plane gates on cellulose-nanofiber-soaked papers. *Adv. Electron. Mater.* **5**, 1900235 (2019).
- Kim, J.-H. *et al.* Flexible ITO films with atomically flat surfaces for high performance flexible perovskite solar cells. *Nanoscale* **10**, 20587–20598 (2018).
- Delahoy, A. E. & Guo, S. In *Handbook of Photovoltaic Science and Engineering* (eds Luque, A. & Hegedus, S.) 716–796 (Wiley, New York, 2011).
- Watson, J. & Castro, G. A review of high-temperature electronics technology and applications. *J. Mater. Sci. Mater. Electron.* **26**, 9226–9235 (2015).
- Medina, D. F. In *Handbook of Cosmic Hazards and Planetary Defense* (eds Pelton, J. N. & Allahdadi, F.) 295–314 (Springer International Publishing, Cham, 2015).
- National Research Council *Materials for High-Temperature Semiconductor Devices* (The National Academies Press, 1995).



9. Varshni, Y. P. Temperature dependence of the energy gap in semiconductors. *Physica* **34**, 149–154 (1967).
10. O'Donnell, K. P. & Chen, X. Temperature dependence of semiconductor band gaps. *Appl. Phys. Lett.* **58**, 2924–2926 (1991).
11. Irmscher, K. *et al.* On the nature and temperature dependence of the fundamental band gap of In<sub>2</sub>O<sub>3</sub>. *Phys. Status Solidi A* **211**, 54–58 (2014).
12. Morris, A. J. & Monserrat, B. Optical absorption driven by dynamical symmetry breaking in indium oxide. *Phys. Rev. B* **98**, 161203 (2018).
13. Fan, J. C. C. & Goodenough, J. B. X-ray photoemission spectroscopy studies of Sn-doped indium-oxide films. *J. Appl. Phys.* **48**, 3524–3531 (1977).
14. Hamberg, I. & Granqvist, C. G. Evaporated Sn-doped In<sub>2</sub>O<sub>3</sub> films: Basic optical properties and applications to energy-efficient windows. *J. Appl. Phys.* **60**, R123–R160 (1986).
15. Müller, H. K. Electrical and optical properties of sputtered In<sub>2</sub>O<sub>3</sub> films. I. Electrical properties and intrinsic absorption. *Phys. Status Solidi B* **27**, 723–731 (1968).
16. Ginley, D. S., Hosono, H. & Paine, D. C. *Handbook of Transparent Conductors* (Springer, New York, 2010).
17. Madan, A. & Shaw, M. P. In *The Physics and Applications of Amorphous Semiconductors* (eds Madan, A. & Shaw, M. P.) 1–10 (Academic Press, London, 1988).
18. Kim, J.-W. *et al.* Atomistic aspects of carrier concentration variation in post-annealed indium tin oxide films. *J. Phys. D Appl. Phys.* **48**, 395307 (2015).
19. Paine, D. C. *et al.* A study of low temperature crystallization of amorphous thin film indium–tin–oxide. *J. Appl. Phys.* **85**, 8445–8450 (1999).
20. Ziman, J. M. *Electrons and Phonons: The Theory of Transport Phenomena in Solids* (Oxford University Press, Oxford, 2001).
21. Taga, N. *et al.* Electrical properties of heteroepitaxial grown tin-doped indium oxide films. *J. Appl. Phys.* **80**, 978–984 (1996).
22. Nistor, M., Gherendi, F. & Perrière, J. Degenerate and non-degenerate In<sub>2</sub>O<sub>3</sub> thin films by pulsed electron beam deposition. *Mater. Sci. Semicond. Process.* **88**, 45–50 (2018).
23. Nistor, M., Seiler, W., Hebert, C., Matei, E. & Perrière, J. Effects of substrate and ambient gas on epitaxial growth indium oxide thin films. *Appl. Surf. Sci.* **307**, 455–460 (2014).
24. Chatratin, I. *et al.* Role of point defects in the electrical and optical properties of In<sub>2</sub>O<sub>3</sub>. *Phys. Rev. Mater.* **3**, 074604 (2019).
25. Buckeridge, J. *et al.* Deep vs shallow nature of oxygen vacancies and consequent *n*-type carrier concentrations in transparent conducting oxides. *Phys. Rev. Mater.* **2**, 054604 (2018).
26. Jiang, X. B., Jiang, M. & Zhao, M. Thermodynamic understanding of phase transitions of In<sub>2</sub>O<sub>3</sub> nanocrystals. *Chem. Phys. Lett.* **563**, 76–79 (2013).
27. Fujita, S. & Kaneko, K. Epitaxial growth of corundum-structured wide band gap III-oxide semiconductor thin films. *J. Cryst. Growth* **401**, 588–592 (2014).
28. Ohta, H. *et al.* Highly electrically conductive indium–tin–oxide thin films epitaxially grown on yttria-stabilized zirconia (100) by pulsed-laser deposition. *Appl. Phys. Lett.* **76**, 2740–2742 (2000).
29. Gruenewald, J. H., Nichols, J. & Seo, S. S. A. Pulsed laser deposition with simultaneous in situ real-time monitoring of optical spectroscopic ellipsometry and reflection high-energy electron diffraction. *Rev. Sci. Instrum.* **84**, 043902 (2013).
30. Guerette, M. & Huang, L. In-situ Raman and Brillouin light scattering study of the international simple glass in response to temperature and pressure. *J. Non-Cryst. Solids* **411**, 101–105 (2015).
31. Azzam, R. M. A. & Bashara, N. M. *Ellipsometry and Polarized Light* (North-Holland, Amsterdam, 1987).
32. Maulana, L. Z. *et al.* Inexpensive home-made single wavelength ellipsometer ( $\lambda = 633$  nm) for measuring the optical constant of nanostructured materials. *IOP Conf. Ser. Mater. Sci. Eng.* **202**, 012031 (2017).
33. König, T. A. F. *et al.* Electrically tunable plasmonic behavior of nanocube-polymer nanomaterials induced by a redox-active electrochromic polymer. *ACS Nano* **8**, 6182–6192 (2014).

## Acknowledgements

We acknowledge the support of NASA Kentucky under NASA award number NNX15AR69H (for high-temperature optical measurements) and a National Science Foundation grant DMR-1454200 (for thin-film synthesis and characterization). J.K. acknowledges the support from the Global Ph.D. Fellowship Program (2015H1A2A1034200) through the NRF Korea funded by the Ministry of Education.

## Author contributions

J.K. and J.G.C. synthesized the samples. J.K. carried out the X-ray diffraction and optical spectroscopic ellipsometry measurements. S.S., M.S. and S.P. provided technical assistance and scientific advice. J.K. and A.S. analyzed the experimental data, wrote the manuscript, and all authors reviewed it. A.S. conceived the project and supervised its progress for this manuscript.

## Competing interests

The authors declare no competing interests.

## Additional information

**Supplementary information** is available for this paper at <https://doi.org/10.1038/s41598-020-69463-4>.

**Correspondence** and requests for materials should be addressed to A.S.

**Reprints and permissions information** is available at [www.nature.com/reprints](http://www.nature.com/reprints).

**Publisher's note** Springer Nature remains neutral with regard to jurisdictional claims in published maps and institutional affiliations.



**Open Access** This article is licensed under a Creative Commons Attribution 4.0 International License, which permits use, sharing, adaptation, distribution and reproduction in any medium or format, as long as you give appropriate credit to the original author(s) and the source, provide a link to the Creative Commons license, and indicate if changes were made. The images or other third party material in this article are included in the article's Creative Commons license, unless indicated otherwise in a credit line to the material. If material is not included in the article's Creative Commons license and your intended use is not permitted by statutory regulation or exceeds the permitted use, you will need to obtain permission directly from the copyright holder. To view a copy of this license, visit <http://creativecommons.org/licenses/by/4.0/>.

© The Author(s) 2020